Journal of Atmospheric and Solar-Terrestrial Physics 73 (2011) 2153–2165

Contents lists available at ScienceDirect

Journal of Atmospheric and Solar-Terrestrial Physics

journal homepage: www.elsevier.com/locate/jastp

The electron density dependence of polar mesospheric summer echoes

Roger H. Varney [a,*], Michael C. Kelley [a], Michael J. Nicolls [b], Craig J. Heinselman [b], Richard L. Collins [c]

[a] School of Electrical and Computer Engineering, Cornell University, Ithaca, NY, USA
[b] Center for Geospace Studies, SRI International, Menlo Park, CA, USA
[c] Geophysical Institute and Department of Atmospheric Sciences, University of Alaska Fairbanks, Fairbanks, AK, USA

ARTICLE INFO

Article history:
Received 19 February 2010
Received in revised form
7 July 2010
Accepted 19 July 2010
Available online 23 July 2010

Keywords:
Polar mesospheric summer echoes (PMSE)
Poker Flat Incoherent Scatter Radar (PFISR)
Turbulent spectra

ABSTRACT

Many of the expressions for the reflectivity of polar mesospheric summer echoes (PMSE) predict that the echo strength is controlled by the electron density. We present several observations made using the Poker Flat Incoherent Scatter Radar which are difficult to explain based on those expressions, including observations at night with no detectable incoherent scatter below 90 km and during aurora where the reflectivity shows no response to abrupt changes in ionization. We derive a new expression for the reflectivity and are still able to explain all of these observations as scatter from free electrons. When the electron density is much smaller than the ice density the reflectivity is a strong function of electron density. In the opposite limit the reflectivity is solely controlled by the ice density because only a fraction of the electron density variance generated at the largest scales can get convected to sufficiently small scales.

1. Introduction

Much interest in the physics of dusty/icy plasmas has been generated by the observation of strong radar echoes at VHF and UHF from the summer polar mesopause. Since the first observations at ~50 MHz (Czechowsky et al., 1979; Ecklund and Balsley, 1981), observations have been made at 224 MHz (e.g. Röttger et al., 1988, 1990; Rapp et al., 2008), 450 MHz (e.g. Nicolls et al., 2007, 2009; Varney et al., 2009), 500 MHz (e.g. Hall and Röttger, 2001), 933 MHz (e.g. Röttger et al., 1990; Rapp et al., 2008), and even 1295 MHz (e.g. Cho et al., 1992a). These polar mesospheric summer echoes (PMSE) are fundamentally related to the ice grains in mesospheric ice clouds (Rapp and Lübken, 2004), and are thus of interest for both fundamental dusty plasma research and as a tool for monitoring the mesospheric ice clouds, which are believed to be related to anthropogenic atmospheric changes (e.g. Gadsden, 1990). The similarity of the echoes to coherent echoes from mesospheric turbulence (e.g. Røyvick and Smith, 1984) has prompted the notion that turbulence is somehow involved, but the echo strengths at VHF are orders of magnitude stronger than typical mesospheric echoes and normal mesospheric echoes are completely nonexistent at UHF. The first significant step towards a turbulent theory of PMSE was taken by Kelley et al. (1987), who proposed that the electron diffusion in the mesosphere was considerably reduced by the presence of heavy cluster ions. The turbulent spectrum of the density of an additive which has a diffusion rate which is much smaller than the kinematic viscosity of the bulk fluid can be extended to much smaller scales than the velocity spectrum of the turbulent flows themselves (Batchelor, 1959). Thus anomalously low electron diffusion could explain the existence of turbulent mesospheric echoes at UHF scales without needing the turbulence itself to have structure at these scales. In a plasma or weakly ionized gas the diffusion of various charged species are all coupled through long range forces, meaning that the electron diffusion has multiple modes which are characterized by the diffusion of all the larger species (Hill, 1978a; Rapp and Lübken, 2003). Cho et al. (1992b) applied this theory to the summer polar mesopause and proposed that the electron diffusion was characterized by the slowest ambipolar diffusion mode associated with the charged ice grains.

Rocket measurements of neutral turbulence challenged the turbulent theory of PMSE by showing that PMSE was often not collocated with turbulence (Lübken et al., 2002). Furthermore, the original theory of Cho et al. (1992b) required the amount of charge on the dust to be at least equal to the amount of charge on the free electrons (i.e. $\Lambda = |Z_d|N_d/N_e \geq 1$), a condition which is not always met when PMSE is observed (Havnes et al., 2001; Rapp et al., 2002a). Both of these problems were resolved by Rapp and Lübken (2003) who revisited the theory of ambipolar diffusion and showed that the $\Lambda = 1$ condition was a result of faulty initial conditions chosen by Cho et al. (1992b), and that "fossilized" electron density structures can survive for substantial amounts of time after the generating turbulence has disappeared. Nonetheless a few studies are still challenging the turbulent theory of PMSE. PMSE at UHF was once proposed to be a form of enhanced incoherent scatter associated with high charge numbers on the ice

* Corresponding author. Tel.: +1 610 2836658.
E-mail address: rhv5@cornell.edu (R.H. Varney).

1364-6826/$ - see front matter © 2010 Elsevier Ltd. All rights reserved.
doi:10.1016/j.jastp.2010.07.020

grains (Hagfors, 1992; La Hoz, 1992), but studies of the ice charging have shown that the high charge numbers needed for this theory are impossible to obtain (Rapp and Lübken, 2001). Furthermore, Bellan (2008) has recently proposed that PMSE is scatter from metal layers on the ice grains themselves and not from free electrons. According to current microphysical models the formation of metal layers on the ice grains is unlikely and the theory of Bellan (2008) cannot explain the response of PMSE to RF heating (Rapp and Lübken, 2009).

This paper scrutinizes one particular aspect of the turbulent theory of PMSE: the electron density dependence of the echo strength. Several expressions for the reflectivity, i.e. the radar scattering cross section per unit volume, have suggested that the PMSE reflectivity is proportional to

$$\left(\frac{\omega_B^2 N_e}{g}-\frac{dN_e}{dz}-\frac{N_e}{H_n}\right)^2, \quad (1)$$

where ω_B is the Brunt–Vaisala frequency, g is the acceleration due to gravity, H_n is the neutral scale height, and N_e is the electron density (Cho, 1993; Rapp et al., 2008). These expressions predict a strong variation in the strength of PMSE with electron density. Statistical studies of the occurrence frequency of PMSE have noted that PMSE is more often detected near midday and that it is correlated with geomagnetic activity, especially at night (Bremer et al., 2000, 2001; Varney et al., 2009). These trends are easily explained if PMSE reflectivity scales with the electron density.

Section 3 presents several examples of PMSE and aurora observed together with the Poker Flat Incoherent Scatter Radar (PFISR). Dynamic particle precipitation creates order of magnitude fluctuations in electron density on times scales which are much shorter than any of the mesospheric ice cloud parameters are expected to change, and thus provides a perfect opportunity to investigate the electron density dependence of PMSE. Furthermore, observations of PMSE at night with no detectable incoherent scatter from free electrons are discussed. Section 4 reviews the application of models of spectral transfer functions to advected passive scalars in both neutral and ionized gases (Hill, 1978b; Hill and Mitton, 1998; Hill et al., 1999), and derives an asymptotic expression for the reflectivity at high wavenumbers. The asymptotic expression predicts a much more complicated electron density dependence than Eq. (1). Section 5 reinterprets the observations in Section 3 in light of this new expression, and Section 6 makes concluding remarks.

2. Experimental methodology

The Poker Flat Incoherent Scatter Radar (PFISR) is a 450 MHz, 1.7 MW electronically steerable phased array located on the Poker Flat Research Range (PFRR) in Chatanika, Alaska (65.13°N, 147.47°W). Experiments dedicated to PMSE and D-region studies have been conducted during late July and early August in 2008 and 2009. Both radar modes are modified forms of that used in August 2007 by Nicolls et al. (2009). Visibility permitting, lidar measurements were made using the 532 nm NICT Rayleigh lidar at the PFRR (see Collins et al., 2009, for system details). Though early August is near the end of the typical PMSE season, the nighttime sky is dark enough to support high-resolution optical measurements of mesospheric ice clouds (e.g. Collins et al., 2009). While Rayleigh lidars have been designed to make daytime measurements, the NICT Rayleigh lidar is primarily designed to make temperature measurements at night (Thurairajah et al., 2009) and measures mesospheric ice clouds in twilight under clear sky conditions. Both incoherent scatter from the D-region and the coherent scatter from PMSE are spectrally narrow, permitting Doppler spectra to be computed from pulse to pulse correlations. The various experimental parameters for the two experiments are summarized in Table 1. The 2008 mode used five different look directions. It cycled between the four off-vertical beams, but sent every other pulse to the vertical beam. Thus although the IPP was 2 ms, pulses in the same beam which were used for pulse to pulse correlations are 4 ms apart. One hundred and twenty-eight pulses would be sent to an off-vertical beam before switching to a different off-vertical beam. This technique allows the vertical beam to have a much greater statistical accuracy and extremely fine Doppler resolution. The 2009 mode simply cycled through three beams, sending 256 pulses in each direction before switching.

Table 1
Experimental parameters for the 2008 and 2009 PFISR PMSE experiments.

Experimental parameters		
Year	2008	2009
Dates	8/1/08–8/13/08	7/29/09–8/14/09
Number of beams	5	3
Pulse length (μs)	112	240
Pulse length (bauds)	28	60
Baud length (m)	600	600
IPP (ms)	2 (effectively 4)	3
Nyquist frequency (Hz)	125	167
Maximum spectral resolution (Hz)	1 (0.17 vertical)	0.65

The narrow Doppler spectra of the targets also imply that the targets are phase-coherent over the pulse length, which permits the use of binary phase codes for pulse compression. The 2008 experiment uses a 28-baud code which has been used for previous PFISR D-region measurements (1, −1, −1, −1, 1, 1, 1, 1, −1, −1, −1, 1, −1, −1, 1, −1, −1, 1, −1, −1, 1, 1, −1, 1, −1, 1, 1, 1, −1, 1) (Nicolls et al., in press), and the 2009 experiment used a 60-baud code which has never been used on PFISR before (−1, 1, −1, −1, −1, −1, −1, −1, 1, 1, −1, −1, 1, −1, −1, −1, 1, −1, −1, −1, 1, 1, 1, 1, 1, 1, −1, −1, 1, −1, 1, 1, −1, −1, 1, −1, −1, 1, −1, 1, −1, 1, 1, −1, 1, 1, 1, 1, 1, −1, −1, 1, 1, 1, −1, −1, 1, −1, 1, −1, −1, 1, 1). All returns were sampled twice per baud and decoded with a matched filter. Noise estimates are taken from low altitude ranges (typically ∼50−60 km) which are above the ground clutter and below the D-region ionosphere. The 2009 experiment used a longer pulse which created more ground clutter, so noise estimates had to be taken from 65 to 70 km instead, which is still too low for the D-region to be detectable in most circumstances. Signal-to-noise ratios were converted to calibrated reflectivities using system constants derived from detailed plasma line measurements and injected noise calibration pulses from other experiments. The calibration procedure has been described in more detail by Nicolls et al. (2007).

3. Observations

If PMSE is dependent on free electrons then it should be impossible to produce at night when the normal D-region has recombined without some extra source of ionization. Varney et al. (2009) noted that a majority of the nighttime PMSE observed by PFISR in 2007 were accompanied by enhanced E-region ionization from particle precipitation. On August 12, 2009 the NICT Rayleigh lidar at Poker Flat detected a mesospheric ice cloud between 107 and 203 Alaska Standard Time (AKST, UTC-9) and concurrent radar measurements (not shown) contained no signal whatsoever in any look direction, including the common volume vertical beam. This event occurred in darkness with no particle precipitation, so the absence of PMSE is trivially explained by a lack of free electrons. Previous observations of mesospheric ice clouds at

night with lidar during the absence of PMSE have been explained in exactly the same way (von Zahn and Bremer, 1999).

These observations seem to suggest that particle precipitation is a necessary condition for PMSE at night. However, during a nighttime event which has been described in detail by both Taylor et al. (2009) and Kelley et al. (2010), a PMSE was observed during a strong burst of particle precipitation, but the PMSE began several minutes before the detectable ionization extended to the PMSE altitude. Furthermore the reflectivity did not change noticeably after the ionization dramatically increased. The nighttime PMSE presented in Fig. 1 is even more perplexing. PMSE is observed sporadically for 3 h and yet no appreciable incoherent scatter from free electrons is detected in the D-region during the entire event. The electron density in the E-region is at most $2\times10^{10}\,\mathrm{m}^{-3}$. Inside the PMSE layer the electron density is clearly far below PFISR's detection limit for incoherent scatter, but is not necessarily 0. The exact detection limit varies depending on experimental parameters, but is nominally a reflectivity of $\sim10^{-19}\,\mathrm{m}^{-1}$, which corresponds to an electron density of $2\times10^{9}\,\mathrm{m}^{-3}$. Rapp et al. (2002a) have estimated the lower electron density limit for VHF PMSE at a few times $10^{8}\,\mathrm{m}^{-3}$, which is certainly below PFISR's detection limit. Weather conditions prevented the operation of the lidar on this night.

If the PMSE reflectivity simply scaled with electron density according to Eq. (1) then one would expect rapid changes in electron density due to particle precipitation to create rapid changes in reflectivity, creating the appearance of the PMSE being modulated on and off by the aurora. Fig. 2 shows an example of one such event. There is an extremely weak PMSE at 86 km at 720 AKST which becomes noticeably stronger promptly when the aurora strengthens. Additionally there is a double layer of PMSE around 800 AKST which only exists during the strongest part of the particle precipitation. The observations at 933 MHz presented by Rapp et al. (2008) and at 1295 MHz presented by Cho et al. (1992a) both show a similar correlation between the appearance of PMSE and the strengthening of particle precipitation.

At PFISR, however, Fig. 2 is atypical of observations of coincident PMSE and aurora. Fig. 3 shows a rather different example of the two phenomena together. Here the PMSE begins before the aurora strengthens, and shows no response to the particle precipitation. The modulation in altitude and bifurcation into multiple layers indicates some very complicated neutral

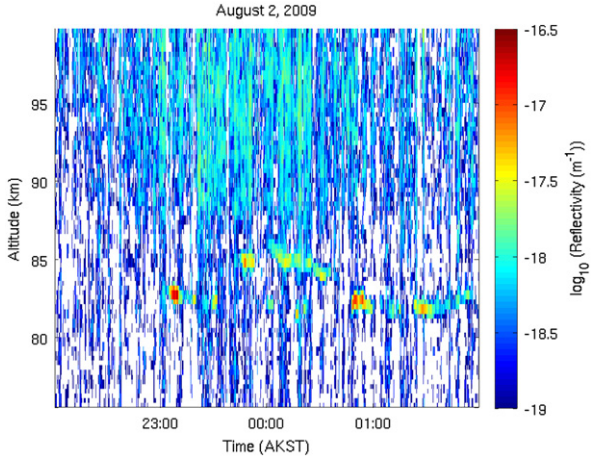

Fig. 1. Calibrated reflectivities for a PMSE observed at night. The times on the abscissa are in Alaska Standard Time (AKST = UTC-9). The color scale corresponds to the $\log_{10}$ of the reflectivity in m^{-1}. For incoherent scatter a reflectivity of $10^{-18}\,\mathrm{m}^{-1}$ corresponds to an electron density of $2\times10^{10}\,\mathrm{m}^{-3}$. Each pixel is 16 s by 300 m and the data have been additionally smoothed using a 48 s running median in time and a 900 m running median in range.

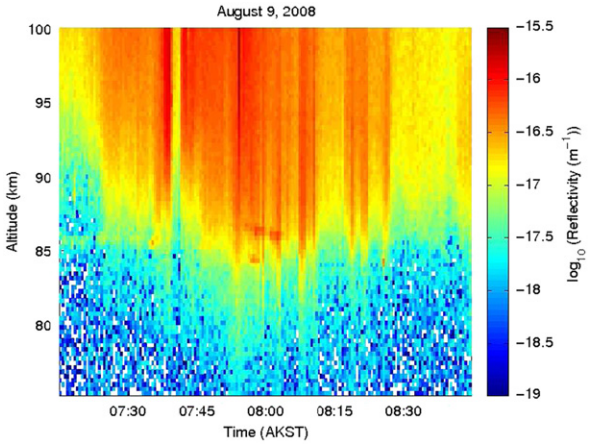

Fig. 2. Calibrated reflectivities for multiple PMSEs observed with aurora. Most of the signal is incoherent scatter associated with particle precipitation. The PMSEs are the narrow layer at 86 km in the beginning of the time period, and the pair of layers around 800 AKST. Each pixel is 30 s by 300 m and no additional filtering was performed.

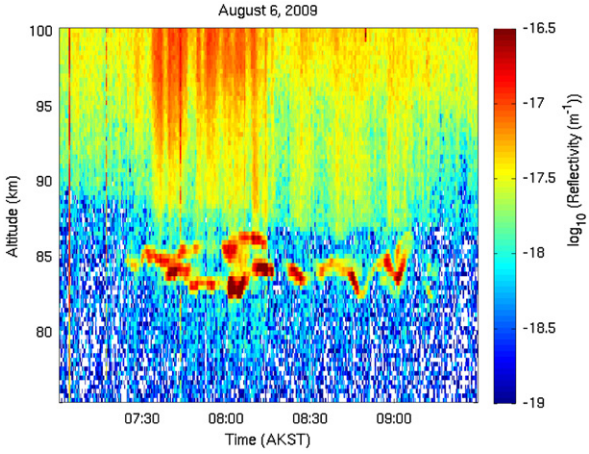

Fig. 3. Calibrated reflectivities for a highly dynamic PMSE during aurora. The PMSE is the highly structured layer or pair of layers centered around 85 km. Each pixel is 16 s by 300 m and the data have been smoothed by a 48 s running median in time.

dynamics are driving this PMSE. Another observation where PMSE occurred with aurora and showed no relationship to the aurora but had much calmer neutral dynamics has been described in detail by Nicolls et al. (2009).

A PMSE which was modulated by aurora and a PMSE which was unaffected by aurora were observed simultaneously on August 10, 2008. Fig. 4 shows the reflectivity and Fig. 5 shows the corresponding spectrograms inside the PMSE layer. At 655 AKST the particle precipitation becomes exceptionally strong and produces detectable ionization as low 70 km. The electron density inside the PMSE layer certainly jumped by an order of magnitude or more at this time. A PMSE at 86 km begins promptly with the increase in ionization. There was another weaker PMSE at this altitude at 615 AKST which is much easier to identify in the spectrogram. This PMSE also coincided with strong particle precipitation and promptly disappeared when the aurora weakened. At 640 AKST a PMSE forms between 84 and 85 km, while the aurora is relatively weak, and after the sudden increase in ionization this layer shows no change in reflectivity whatsoever. The spectral widths before and after the increase in ionization show no change, suggesting that the strength of the driving turbulence stays constant.

During this event the electron density changes dramatically in less than a minute, which is much faster than the properties of the ice grains within the cloud are expected to change. During a numerical simulation of the transport and growth of a large number of ice condensation nuclei by Berger and von Zahn (2002) a single representative grain took 5 h to sublimate from 55 nm back to a bare dust nucleus once it fell sufficiently far below the temperature minimum. This average sublimation rate of 0.18 nm/min is faster than any of the growth rates. Furthermore, what matters is the average grain properties over the layer, not the properties of any individual particle. Even if the grains could respond instantly to changes in the background atmospheric parameters, the fastest source of variation in these parameters is due to high frequency gravity waves whose periods are necessarily longer than the

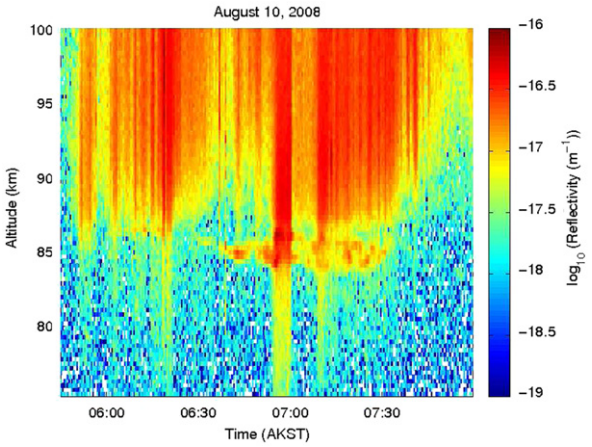

Fig. 4. Calibrated reflectivities for another example of coincident PMSE and particle precipitation. Each pixel is 30 s by 300 m and no additional filtering was performed. The particularly strong precipitation just before 700 AKST creates detectable ionization well below the lower limit of this plot. The upper PMSE layer appears and disappears with fluctuations in the strength of the aurora, but the lower PMSE layer appears to have no interaction with the aurora.

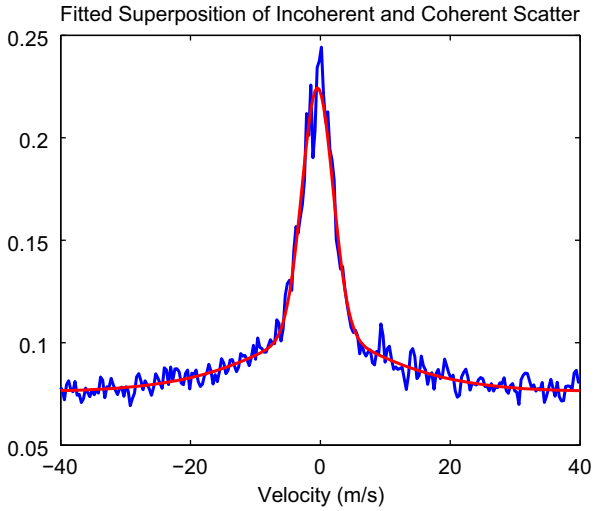

Fig. 6. Integrated spectrum from 85.1 km with a fitted superposition of Gaussian and Lorentzian models. The central portion is Gaussian coherent scatter, and the elevated wings on the spectra are Lorentzian incoherent scatter.

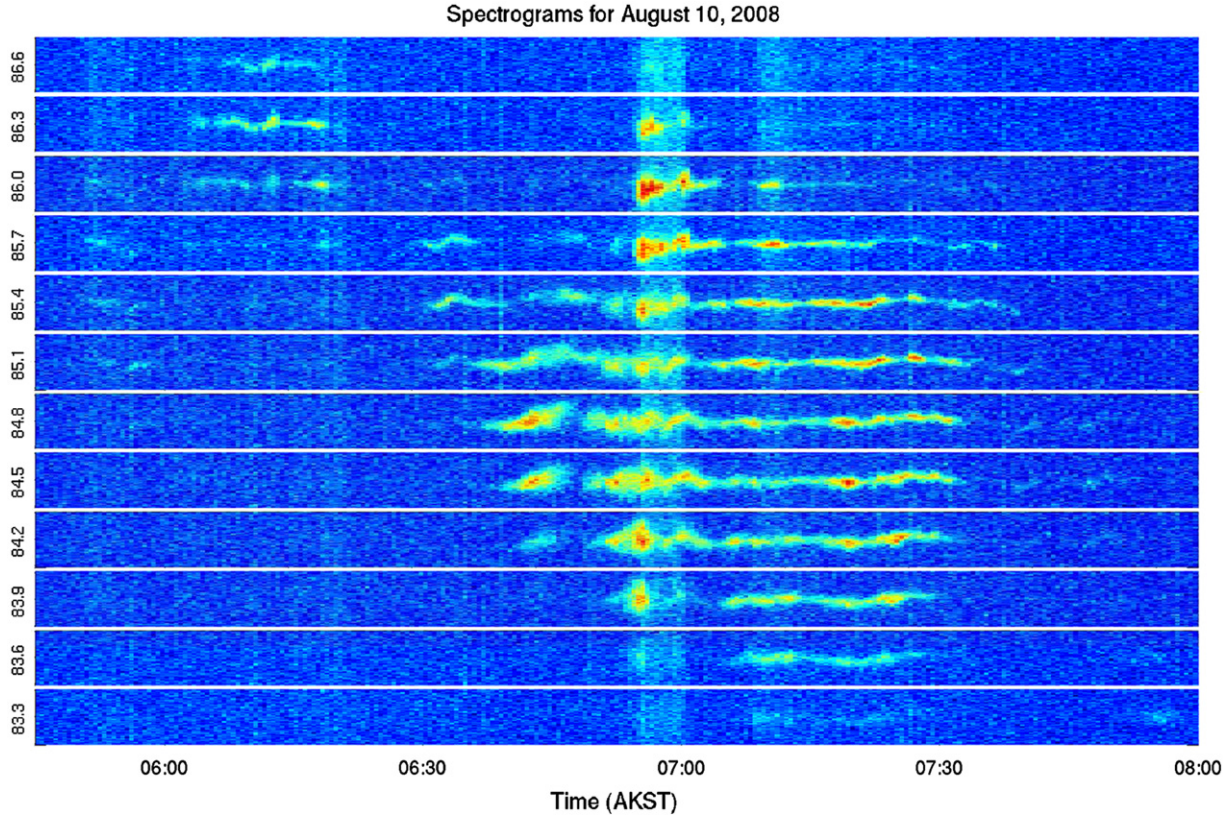

Fig. 5. Doppler spectrograms for the PMSE event depicted in Fig. 4. The altitude corresponding to each spectrogram is indicated on the left side. Only the center portions of the spectra from −10 to 10 m/s are shown. Each pixel is 30 s by 0.33 m/s (1 Hz). The color scale is proportional to the logarithm of the power spectral densities in arbitrary units. The narrow returns near the beginning at higher altitude are PMSE which are difficult to distinguish in Fig. 4, but stand out in the spectra due to their narrow spectral widths. The diffuse light blue spectra are incoherent scatter which is strong enough to be detected with only 30 s of integration.

Brunt–Vaisala period (Hines, 1960), which is typically ~ 5 min in the mesosphere (Lübken, 1999). A more serious concern is the horizontal transport of the particles out of the beam. A 1° beam creates a 1.5 km wide spot at 85 km, meaning that a horizontal wind of only 25 m/s is required for a grain to traverse the beam in 1 min. Nonetheless, the horizontal scales of the cloud should be comparable to the horizontal wavelengths of gravity waves, which are at least 10 km at these altitudes. Waves with smaller horizontal wavelengths are easily reflected at lower altitudes and are thus unimportant at mesospheric and thermospheric heights (Fritts and Alexander, 2003). During this event PMSE with comparable reflectivities and spectral widths were observed in all five look directions. This suggests that the ice grain and turbulence parameters were similar over at least the ~ 30 km beam separation.

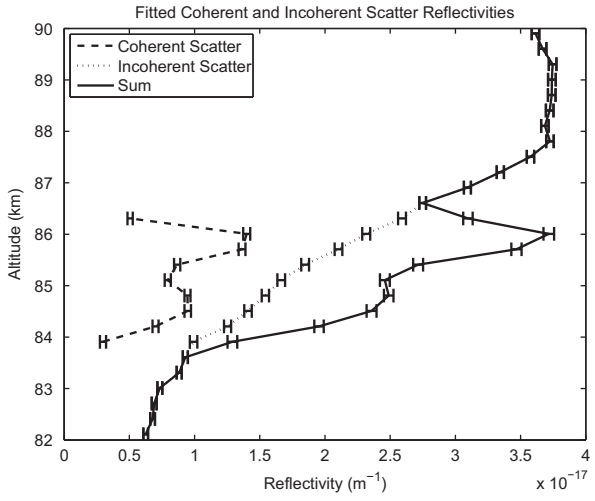

Fig. 7. Calibrated reflectivities from the Gaussian and Lorentzian components of the fits. The strength of the incoherent scatter from inside the PMSE layer shows no measurable depletion. An incoherent scatter reflectivity of $1 \times 10^{-17}\,\mathrm{m}^{-1}$ corresponds to an electron density of $2 \times 10^{11}\,\mathrm{m}^{-3}$.

During the event the D-region electron densities exceed $10^{11}\,\mathrm{m}^{-3}$. This exceptionally high electron density affords the opportunity to derive even more information about the inside of this particular PMSE layer. The light blue around the PMSE in the spectrogram is detectable incoherent scatter. The period of intense ionization from 655 to 700 UT was integrated and then fit with a superposition of a Lorentzian model for the incoherent scatter and a Gaussian model for the coherent scatter. An example of one such fitted spectrum is shown in Fig. 6. The center of the spectrum has a distinctly Gaussian shape, but the incoherent scatter is strong enough to fit a Lorentzian to the higher frequency wings. The spectra immediately above and below the PMSE layer were fit with a single Lorentzian model. The Lorentzian model used ignores the broading of the spectrum due to turbulence. The turbulence broadening could be included by using a Voigt spectrum, the convolution of a Lorentzian and Gaussian (Nicolls et al., in press). The amplitudes of the two fitted components can be calibrated independently, yielding the simultaneous measurements of the reflectivities of the incoherent and coherent scatter component plotted in Fig. 7. The reflectivity of the incoherent scatter component can be converted to electron density in m^{-3} by multiplying by 2×10^{28} assuming the electron and ion temperatures are equal, the Debye length is much smaller than the Bragg scale, and the ion density is much greater than the dust density. No biteout in the electron density caused by electron capture by ice grains is observed, but this is not surprising for these exceptionally high electron densities. Recent optical measurements from the SOFIE instrument on the AIM satellite show average ice grain densities of $2\text{–}6 \times 10^{8}\,\mathrm{m}^{-3}$ throughout the middle of the ice layer, with densities in parts of the layer sometimes exceeding $10^{9}\,\mathrm{m}^{-3}$ (Hervig et al., 2009). Rocket measurements have shown charge number densities of $|Z_d|N_d = 1-3 \times 10^{9}\,\mathrm{m}^{-3}$ (Havnes et al., 1996; Robertson et al., 2009). Usually this is a significant fraction of the total electron density, but in this case the electron density is over $10^{11}\,\mathrm{m}^{-3}$, and

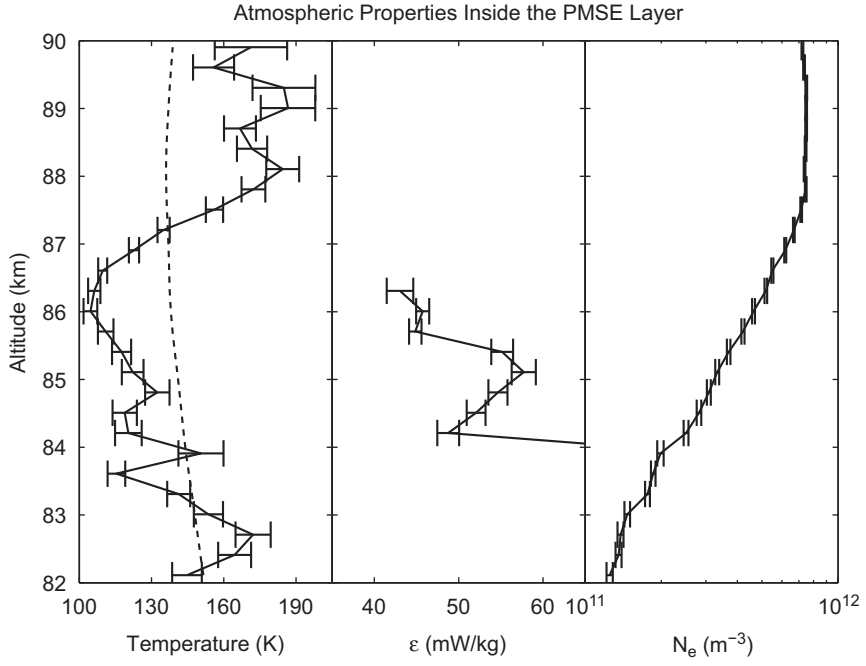

Fig. 8. Profiles of temperature derived from the Lorentzian spectral width (left), energy dissipation rates derived from the Gaussian spectral width (center), and electron density from the calibrated size of the Lorentzian component (right). The extra dashed line in the temperature plot is the temperature profile suggested by Lübken (1999) for the second week of August.

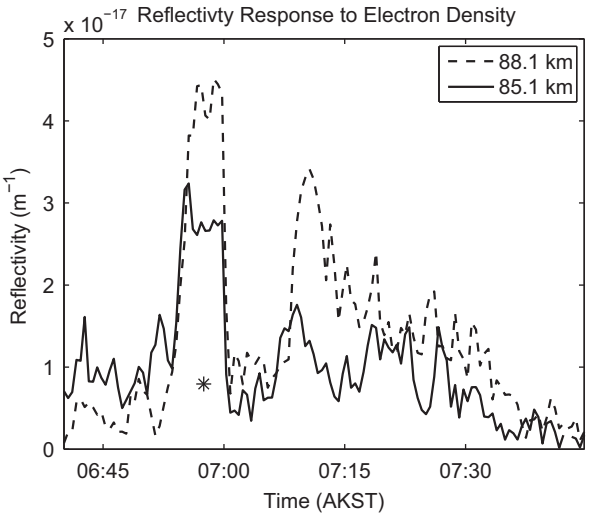

Fig. 9. Time series of the reflectivity inside the PMSE layer (85.1 km), and immediately above the PMSE layer (88.1 km). The black astrix is the coherent scatter portion of the reflectivity at 85.1 km between 655 and 700 AKST taken from Fig. 7. This coherent scatter reflectivity is nearly identical to the earlier total reflectivities at this altitude, demonstrating that apparent correlations between the reflectivities from the two altitudes are entirely due to changes in the incoherent scatter contributions.

thus the expected biteout is much smaller than the errorbars on the density measurements.

The half power half widths of the Lorentzian components of the spectra are given by (Dougherty and Farley, 1963)

$$\gamma = \frac{16\pi k_B T}{\lambda_R^2 m_i \nu_{in}}, \tag{2}$$

where k_B is Boltzmann's constant, T is the plasma temperature (which is equal to the neutral temperature for all species in the highly collisional limit), λ_R is the radar wavelength, m_i is the ion mass, and ν_{in} is the ion-neutral momentum transfer collision frequency. The temperatures plotted in the left panel of Fig. 8 are derived from these spectral widths assuming an ion mass of 31 amu, computing collision frequencies using an expression from Hill and Bowhill (1977) and using neutral densities from the NRLMSISE-00 model (Hedin, 1991; Picone et al., 2002). For comparison the temperature profile suggested by Lübken (1999) for the second week in August is also plotted. The temperatures from Lübken (1999) are consistently lower than the NRLMSISE-00 model, and lidar studies at Poker Flat have shown that the formation of mesospheric ice clouds is more consistent with the temperatures from Lübken (1999) than those from NRLMSISE-00 (Collins et al., 2003). The departure of the measured temperatures from this model may be partially an artifact of assuming an ion mass of 31 amu throughout the layer, but could also represent true variability due to internal gravity waves (e.g. Rapp et al., 2002b). Given the complexity of the chemistry of this region various ions heavier than 31 amu may exist, but no lighter ions are expected (e.g. Burns et al., 1991; del Pozo et al., 1997). Thus these temperature estimates should be interpreted as lower bounds for the true temperatures. The energy dissipation rate of the turbulence can be estimated from the widths of the Gaussian components of the spectra using

$$\varepsilon = 9.8\sigma_v^2 \,\mathrm{mW/kg}, \tag{3}$$

where σ_v^2 is the velocity variance (Hocking, 1985). This consistently yields $\sim 50\,\mathrm{mW/kg}$ throughout the layer, except at the lowest altitude where the fit is probably spurious. The variances of the fitted spectral widths and amplitudes were estimated from the Jacobian matrix produced by the Levenberg–Marquart routine used for fitting. These variances were then propagated through the equations for the temperature, energy dissipation rate, and electron density to produce the errorbars in Fig. 8.

The separation of the incoherent and coherent scatter contributions to the reflectivity permits a quantitative demonstration of the response of the coherent scatter to changes in electron density. Fig. 9 shows times series of the reflectivity from an altitude immediately above the PMSE layer and an altitude within the PMSE layer. The reflectivity from the higher altitude is used as a proxy for the electron density inside the PMSE layer since the technique described above for separating the incoherent scatter from the coherent scatter is only possible when the electron density is high. The electron density at the higher altitude is certainly higher than the density inside the PMSE layer, but the variability of the density at this altitude should be indicative of the variability inside the layer. The reflectivity from the lower altitude does show substantial correlations with the higher altitude, but this is entirely due to the incoherent scatter portion of the reflectivity. The black astrix shows the coherent scatter portion of the reflectivity at this altitude obtained from the fitting procedure described above. This value is nearly identical to that of the total reflectivity before the sudden increase in electron density. During periods where the electron density is low the total reflectivity from the PMSE altitude is almost entirely coherent scatter. Thus the coherent scatter reflectivity remains nearly constant throughout the event.

4. Radar scattering cross sections from spectral transfer function theory

The strength of radar echoes is related to the power spectrum of index of refraction fluctuations at one particular vector wavenumber. The radar scattering cross section per unit volume of a medium with stochastic index of refraction fluctuations is given by

$$\eta(\mathbf{k}) = \frac{\pi}{2} k^4 \sin^2\delta \Phi_n(\mathbf{k}), \tag{4}$$

where $\mathbf{k} = \mathbf{k_s} - \mathbf{k_i}$ is the Bragg scattering wavevector, δ is the angle between the incident and scattered wavevectors, and $\Phi_n(\mathbf{k},\omega)$ is the power spectral density of the index of refraction fluctuations normalized such that the integral over all wavenumbers is the total variance of the fluctuations (e.g. Tatarski, 1961; Ottersten, 1969; Hocking, 1985). For a backscatter radar at wavelength λ_R the Bragg wavenumber is simply $k = 4\pi/\lambda_R$ and $\sin^2\delta = 1$. At altitudes where there are free electrons the index of refraction is strongly controlled by the electron density, meaning that Eq. (4) can be rewritten in terms of the spectrum of electron density fluctuations, $\Phi_e(\mathbf{k})$ (e.g. Hocking, 1985):

$$\eta(\mathbf{k}) = 32\pi^4 r_e^2 \Phi_e(\mathbf{k}). \tag{5}$$

Here r_e is the classical electron radius. For isotropic electron density fluctuations it is common to define a one-dimensional power spectrum, $\Gamma_e(k)$, which is the average of $\Phi_e(\mathbf{k})$ over spherical shells in k-space of radius k;

$$\Gamma_e(k) = \int\int_\Omega \Phi_e(\mathbf{k})\, d\Omega = 4\pi k^2 \Phi_e(k), \tag{6}$$

where the second equality assumes isotropy. For isotropic fluctuations the reflectivity can be expressed as

$$\eta(k) = 8\pi^3 r_e^2 k^{-2} \Gamma_e(k). \tag{7}$$

A minor neutral constituent which is advected by turbulence is described by equations of continuity and momentum:

$$\frac{\partial N}{\partial t} + \mathbf{V}\cdot\nabla N = -N\nabla\cdot\mathbf{V}, \tag{8}$$

$$0 = -k_B T \nabla N - m\nu N \mathbf{V}_{rel}, \tag{9}$$

where N, $\mathbf{V}$ and T are the density, velocity and temperature of minor species, k_B is Boltzmann's constant, m is the mass of each particle, and ν is the momentum transfer collision frequency between the minor species and the bulk species. If the velocity of the bulk fluid is divergence free then the divergence of the velocity of the minor species relative to the bulk species, $\mathbf{V}_{rel}$, is the same as the divergence of the absolute velocity of the minor species. Thus Eqs. (8) and (9) can be combined as

$$\frac{\partial N}{\partial t} + \mathbf{V} \cdot \nabla N = D\nabla^2 N, \tag{10}$$

where the diffusion coefficient is defined as $D = k_B T/m\nu$. Fourier transforming this equation in space then multiplying by the Fourier transform of N results in an equation for the power spectrum, $\Phi = N^*(k)N(k)$. Averaging this equation over spherical shells yields an equation in terms of the one-dimensional power spectrum, $\Gamma(k)$ (Hill, 1978b):

$$\frac{\partial \Gamma(k)}{\partial t} - T(k) = -2k^2 D\Gamma(k). \tag{11}$$

The function $T(k)$ arises from the nonlinear term in Eq. (10) and is thus related to the third order moment of N. The nonlinearity means that equations for any moment of N will include terms related to the next higher order moment, and thus the problem can never be closed (Hill and Bowhill, 1976). To proceed a model of $T(k)$ must be used. Only the nonlinear terms can couple together Fourier components at different wavenumbers, and thus $T(k)$ represents the variance which is cascading between scales. For this reason it is called the spectral transfer function and can be expressed in terms of a spectral flux function, $F(k)$ (Hill, 1978b):

$$T(k) = -\frac{\partial F(k)}{\partial k}. \tag{12}$$

Hill (1978b) has thoroughly compared many different possible models of $T(k)$. At the present we shall assume stationarity so that the time derivative can be ignored and assume that the flux is proportional to the power spectrum itself, i.e. $F(k) = s(k)\Gamma(k)$. Corrsin (1964) has recommended flux functions of this form with $s(k) = k/\tau(k)$, where $\tau(k)$ is a characteristic time of the variance cascade to higher wavenumbers, as a continuous generalization of the energy cascade concept proposed by Onsager (1949). The spectrum $\Gamma(k)$ is then the solution to an ordinary differential equation (ODE) of the form

$$\frac{\partial}{\partial k}[s(k)\Gamma(k)] = -2k^2 D\Gamma(k). \tag{13}$$

Traditionally turbulent spectra are divided into a series of subranges based on which physical processes are dominant. For a velocity spectrum the highest wavenumber portion of the spectrum where viscosity is dissipating energy is known as the viscous subrange. Below this is the inertial subrange where energy cascades to progressively higher wavenumbers without being dissipated. The scale marking the transition from the inertial to viscous subranges is proportional to the Kolmogorov microscale, $\eta_K = (\nu_a^3/\varepsilon)^{1/4}$, where ε is the energy dissipation rate and ν_a is the kinematic viscosity of air. Similarly the spectra of minor neutral constituents are divided into diffusive subranges where diffusion is dissipating the scalar variance and convective subranges where the scalar variance is cascading to higher wavenumbers without being dissipated. When the diffusivity is smaller than the viscosity the three principle subranges are the inertial-convective, where both energy and variance are cascading to higher wavenumbers, the viscous-convective, where viscosity is dissipating energy, but the variance is still cascading to higher wavenumbers, and the viscous-diffusive, where both energy and variance are being dissipated. The transition from the viscous-convective to the viscous-diffusive subranges is proportional to the Batchelor microscale, $\eta_B = (\nu_a D^2/\varepsilon)^{1/4} = \eta_K/\sqrt{Sc}$. The dimensionless number $Sc = \nu_a/D$ is called the Schmidt number (e.g. Batchelor, 1959; Hill, 1978b).

In a convective subrange the spectral flux must equal the rate of dissipation of variance at the smallest scales, χ, because variance in a convective subrange will cascade to higher wavenumbers without dissipation. Thus the appropriate boundary condition for Eq. (13) is

$$\lim_{k\to 0} s(k)\Gamma(k) = \chi. \tag{14}$$

In steady state the dissipation of variance, χ, can be equated to the production of variance at the largest scales, i.e.

$$\chi = f_\alpha D\langle(\nabla N')^2\rangle = f_\alpha K(\nabla\langle N\rangle)^2 \tag{15}$$

(Tatarski, 1961), where $\langle\ \rangle$ denotes an average over the turbulent layer, K is the turbulent diffusion coefficient, and the proportionality constant f_α is approximately 2 (Hill and Clifford, 1978). Following Rapp et al. (2008) the second equality can be written as

$$\chi = f_\alpha \frac{Ri\varepsilon}{Pr^t\omega_B^2}(\nabla\langle N\rangle)^2, \tag{16}$$

where ε is the energy dissipation rate, Ri is the Richardson number, Pr^t is the turbulent Prandtl number, and ω_B is the Brunt–Vaisala frequency. Lübken (1992) and Rapp et al. (2008) suggest $Ri = 0.81$, $Pr^t = 1.0$, and a buoyancy period of 5 min as nominal values for the mesosphere. The gradient of the mean density can be expressed in terms of the density, density gradient, and neutral scale height, H_n, via (Hocking, 1985)

$$\nabla\langle N\rangle \equiv M \approx \left(\frac{\omega_B^2 N}{g} - \frac{dN}{dz} - \frac{N}{H_n}\right). \tag{17}$$

In the inertial-convective subrange the energy cascade may only depend on the energy dissipation rate and the wavenumber, so dimensional analysis yields a characteristic time of $\tau(k) = \beta\varepsilon^{-1/3}k^{-2/3}$, which corresponds to $s(k) = \beta^{-1}\varepsilon^{1/3}k^{5/3}$, where $\beta = 0.72$ is the Obukhov–Corrsin constant. Substitution of this form for $s(k)$ into Eq. (13) produces a Kolmogorov inertial subrange with a $k^{-5/3}$ power law (Pao, 1965; Hill, 1978b). Similar dimensional arguments for the viscous-convective and viscous-diffusive subranges result in $s(k) = -\gamma k$, where γ is the effective rate of strain of Kolmogorov eddies (Pao, 1965; Hill, 1978b);

$$\gamma = -\frac{1}{q}\sqrt{\frac{\varepsilon}{\nu_a}}, \tag{18}$$

where Batchelor's constant, q, is a positive dimensionless constant which must be determined from comparison with experiment. Batchelor (1959) estimated q as ~ 2, and Gibson (1968) has placed this value anywhere from $\sqrt{3}$ to $2\sqrt{3}$. For $s(k) = -\gamma k$ the solution to Eq. (13) subject to Eq. (14) is identical to the classic result of Batchelor (1959):

$$\Gamma(k) = -\frac{\chi}{\gamma}k^{-1}\exp\left(\frac{Dk^2}{\gamma}\right). \tag{19}$$

The second model proposed by Hill (1978b) merges the two models above by creating a smooth transition between the inertial and viscous subranges

$$s(k) = \beta^{-1}\varepsilon^{1/3}k^{5/3}\left[\left(\frac{k}{k^*}\right)^{2a} + 1\right]^{-1/(3a)}. \tag{20}$$

The transition is centered at k^* and has a width determined by a. This model will approach $-\gamma k$ at high k for $q = \beta(k^*\eta_K)^{-2/3}$. By comparison with experiment Hill (1978b) estimated $k^*\eta_K = 0.074$ and $a = 1.4$, which correspond to $q = 4.08$ instead of 2. For consistency we will use $q = 4.08$ for the remainder of this paper.

Before these various spectral transfer function models can be applied to PMSE the continuity equations for the various plasma

species must be rederived including the ambipolar electric field in the momentum equation. The relevant continuity and momentum equations for plasma species α are

$$\frac{\partial N_\alpha}{\partial t} + \mathbf{V}_\alpha \cdot \nabla N_\alpha = -N_\alpha \nabla \cdot \mathbf{V}_\alpha, \tag{21}$$

$$0 = q_\alpha N_\alpha \mathbf{E} - k_B T \nabla N_\alpha - m_\alpha \nu_\alpha N_\alpha \mathbf{V}_{\alpha,rel}. \tag{22}$$

Combining these equations, assuming zero net current, and taking the electron mobility and diffusivity to be much greater than that of any other species yields an expression for the ambipolar electric field (Hill, 1978a; Rapp and Lübken, 2003):

$$\mathbf{E} = -\frac{k_B T}{e N_e} \nabla N_e. \tag{23}$$

The electron density can be expressed in terms of the densities of all other species using the quasineutrality condition

$$N_e = \sum_{\beta \neq e} Z_\beta N_\beta. \tag{24}$$

Here $Z_\beta = q_\beta / e$ is the signed number of elementary charges on each particle of species β. Combining Eqs. (24), (23), (22) and (21) and linearizing yields a continuity equation for each plasma species (Hill and Mitton, 1998; Hill et al., 1999):

$$\frac{\partial N_\alpha'}{\partial t} + \mathbf{V}_\alpha \cdot \nabla N_\alpha' = D_\alpha \nabla^2 N_\alpha' + D_\alpha \frac{N_{\alpha 0}}{N_{e0}} Z_\alpha \sum_{\beta \neq e} Z_\beta \nabla^2 N_\beta'. \tag{25}$$

The subscript 0 denotes a mean quantity and primes denote small perturbations about those means. Fourier transforming in space then multiplying the result by the Fourier transform of the density perturbations of species γ yields an expression for the cospectrum, $\Phi_{\alpha\gamma}(\mathbf{k}) = \Re\{N_\gamma^*(k) N_\alpha(k)\}$. Assuming isotropy and integrating over spherical shells in k-space transforms this expression into an expression for the one-dimensional cospectra, $\Gamma_{\alpha\gamma}(k)$ (Hill and Mitton, 1998; Hill et al., 1999):

$$\frac{\partial \Gamma_{\alpha\gamma}(k)}{\partial t} - T_{\alpha\gamma}(k) = -k^2 (D_\alpha + D_\gamma) \Gamma_{\alpha\gamma}(k) - k^2 \sum_{\beta \neq e} [D_\alpha f_{\alpha\beta} \Gamma_{\gamma\beta}(k) + D_\gamma f_{\gamma\beta} \Gamma_{\alpha\beta}(k)], \tag{26}$$

$$f_{\alpha\beta} \equiv Z_\alpha Z_\beta \frac{N_{\alpha 0}}{N_{e0}}. \tag{27}$$

Note that the subscript order is irrelevant for $\Phi_{\alpha\beta}$ and $\Gamma_{\alpha\beta}$, but not for $f_{\alpha\beta}$. As before, the time derivative will be neglected by assuming stationarity and the spectral transfer function $T_{\alpha\gamma}$ will be modeled as

$$T_{\alpha\gamma}(k) = -\frac{\partial}{\partial k}[s(k) \Gamma_{\alpha\gamma}(k)]. \tag{28}$$

This is a set of $n(n+1)/2$ coupled ODEs, where n is the number of plasma species other than electrons, which define the spectra and cospectra of all the non-electron species. The electron spectrum can be obtained from all of these spectra by Fourier transforming the quasineutrality condition

$$\Gamma_e(k) = \sum_{\alpha \neq e} \sum_{\gamma \neq e} Z_\alpha Z_\gamma \Gamma_{\alpha\gamma}(k). \tag{29}$$

Hill and Mitton (1998) and Hill et al. (1999) present numerical solutions to this system of ODEs using the model in Eq. (20) and setting the boundary conditions by assuming each species approaches a normal inertial subrange in the low wavenumber limit, i.e.

$$\Gamma_{\alpha\gamma}(k) = \beta \varepsilon^{-1/3} \chi_{\alpha\gamma} k^{-5/3}. \tag{30}$$

For the purpose of PMSE at VHF and UHF wavenumbers the transition region between the inertial and viscous subrange is unimportant, so the complexity of Eq. (20) is unnecessary. If the simple $s(k) = -\gamma k$ model is used instead then the system can be solved analytically. If the spectra and cospectra of all the non-electron species are arranged in a column vector $\mathbf{\Gamma}$ then the system can be written as a matrix equation of the form

$$\frac{\partial}{\partial k}[k\mathbf{\Gamma}(k)] = 2\frac{k^2}{\gamma}\mathbf{D}\mathbf{\Gamma}(k). \tag{31}$$

The substitutions $\mathbf{W} = k\mathbf{\Gamma}$ and $x = k^2/\gamma$ transform this into an equation of the form

$$\frac{d\mathbf{W}(x)}{dx} = \mathbf{D}\mathbf{W}(x), \tag{32}$$

which is then straightforward to solve by diagonalizing the constant matrix $\mathbf{D}$. The solution is

$$\mathbf{\Gamma}(k) = k^{-1}\mathbf{S}\mathbf{E}(k)\mathbf{C}, \tag{33}$$

where $\mathbf{C}$ is a column vector which must be determined from boundary conditions, $\mathbf{E}$ is a diagonal matrix whose diagonal entries are of the form $\exp(\tilde{D}_i k^2/\gamma)$, where the $\tilde{D}_i$ are the eigenvalues of $\mathbf{D}$, and the columns of $\mathbf{S}$ are the corresponding normalized eigenvectors. By analogy with Eq. (14), the appropriate boundary condition is

$$\lim_{k \to 0} -\gamma k \mathbf{\Gamma} = \boldsymbol{\chi}, \tag{34}$$

where $\boldsymbol{\chi}$ is a column vector containing the various $\chi_{\alpha\gamma}$. Solving for $\mathbf{C}$ using this condition yields the complete solution

$$\mathbf{\Gamma}(k) = -\frac{k^{-1}}{\gamma}\mathbf{S}\mathbf{E}(k)\mathbf{S}^{-1}\boldsymbol{\chi}. \tag{35}$$

Clearly this equation is a generalization of Eq. (19) and the eigenvalues of $\mathbf{D}$ are the effective diffusion coefficients for each of the eigenmodes.

In the case of a single ion species, denoted by a subscript i, and a single dust/ice species, denoted by subscript d, $\mathbf{\Gamma}(k)$ and $\mathbf{D}$ can be written as

$$\mathbf{\Gamma}(k) = \begin{pmatrix} \Gamma_{ii}(k) \\ \Gamma_{id}(k) \\ \Gamma_{dd}(k) \end{pmatrix}, \tag{36}$$

$$\mathbf{D} = \begin{pmatrix} D_i' & D_i' h_i & 0 \\ D_d' h_d/2 & (D_i' + D_d')/2 & D_i' h_i/2 \\ 0 & D_d' h_d & D_d' \end{pmatrix}, \tag{37}$$

where

$$D_i' \equiv D_i(1 + f_{ii}), \quad D_d' \equiv D_d(1 + f_{dd}),$$

$$h_i \equiv \frac{f_{id}}{1 + f_{ii}}, \quad h_d \equiv \frac{f_{di}}{1 + f_{dd}}.$$

In this case the three eigenvalues are

$$\tilde{D}_1 = \frac{D_i' + D_d'}{2} + \frac{1}{2}\sqrt{D_i'^2 + D_d'^2 + D_i' D_d' (4 h_i h_d - 2)}, \tag{38}$$

$$\tilde{D}_2 = \frac{D_i' + D_d'}{2}, \tag{39}$$

$$\tilde{D}_3 = \frac{D_i' + D_d'}{2} - \frac{1}{2}\sqrt{D_i'^2 + D_d'^2 + D_i' D_d' (4 h_i h_d - 2)}, \tag{40}$$

where $\tilde{D}_1 \equiv D_1^0$ and $\tilde{D}_3 \equiv D_2^0$ are commonly called the fast and slow ambipolar modes. In the case of negatively charged dust the expressions above for $D_{1,2}^0$ are equivalent to those derived by Rapp and Lübken (2003). Clearly the third eigenvalue is much smaller than any of the others, so the entry in $\mathbf{E}(k)$ corresponding to this eigenvalue will extend to much smaller scales. An expression for the electron spectrum in the high wavenumber limit is thus obtained by only retaining this term in $\mathbf{E}(k)$ and applying Eq. (29),

$$\Gamma_e(k) = -\frac{\chi_{eff}}{\gamma} k^{-1} \exp\left(\frac{D_2^0 k^2}{\gamma}\right), \tag{41}$$

$$\chi_{eff} = (Z_i^2 \;\; 2Z_iZ_d \;\; Z_d^2)\mathbf{S}\begin{pmatrix}0&0&0\\0&0&0\\0&0&1\end{pmatrix}\mathbf{S}^{-1}\boldsymbol{\chi}, \tag{42}$$

$$\approx Z_d^2\left(\frac{N_e}{N_e+Z_i^2N_i}\right)^2\chi_{dd}, \tag{43}$$

where the approximate form for χ_{eff} is obtained by omitting all terms of order D_d'/D_i' or smaller. When this approximation is made only terms involving the dissipation of dust variance, χ_{dd}, remain. Combining Eqs. (41) and (43) with Eqs. (16), (17) and (7) results in a new expression for PMSE reflectivity

$$\eta(k) = 8\pi^3 r_e^2 \frac{f_\alpha qRi}{Pr^t\omega_B^2}\sqrt{\varepsilon\nu_a}\overline{S}^2\tilde{M}^2k^{-3}\exp\left(\frac{-q(\eta_K k)^2}{Sc}\right), \tag{44}$$

$$\overline{S} \equiv Z_d\left(\frac{N_e}{N_e+Z_i^2N_i}\right), \tag{45}$$

$$\tilde{M} \equiv \left(\frac{\omega_B^2N_d}{g}-\frac{dN_d}{dz}-\frac{N_d}{H_n}\right), \tag{46}$$

$$Sc \equiv \frac{\nu_a}{D_2^0}. \tag{47}$$

Physically $\tilde{M} \equiv \nabla\langle N_d\rangle$ is the gradient of mean dust density across the turbulent layer and $\overline{S}$ is the dust charge times the average number of electrons in each ion Debye sphere.

5. Discussion

The expression derived by Rapp et al. (2008) is identical to Eqs. (41) and (44) with χ_{eff} replaced by the dissipation of electron variance, χ_{ee}. Equating χ_{eff} to χ_{ee} is essentially the result of applying the boundary conditions incorrectly. If one assumes that the boundary condition is

$$\lim_{k\to 0} -\gamma k\Gamma_e(k) = \chi_{ee} \tag{48}$$

and applies this to Eq. (41) to solve for χ_{eff}, then the result is $\chi_{eff} = \chi_{ee}$. However, the approximation leading to Eq. (41), i.e. neglecting the other eigenmodes, is not valid in the low wavenumber limit. When the other eigenmodes decay to 0 they are dissipating some of the variance generated at the largest scales, and only a portion of the variance generated at the largest scales actually gets convected out to the smallest scales. The proper way to apply the boundary condition is to apply Eq. (34) with all of the eigenmodes included, as was done in deriving Eq. (35), and then to take the high wavenumber limit. Nonetheless, Eq. (44) still predicts the same ratio of reflectivities between two radars making common volume measurements at different frequencies. Thus the techniques for estimating the Schmidt number from multiple wavelength observations used by Rapp et al. (2008) and Li et al. (2010) are still useful.

Fig. 10 shows four different examples of numerical solutions to Eq. (31) with one species of positive ion and one species of dust using the complicated model in Eq. (20) for $s(k)$. In each case the spectra were initialized using Eq. (30) at the smallest wavenumber then integrated towards higher wavenumbers using a fourth order Runge–Kutta algorithm. Each $\chi_{\alpha\gamma}$ is determined from Eqs. (16) and (17) assuming the scale height of every species and of the neutrals is 1 km inside the layer. The four examples all use 30 nm particles with a number density of $10^9\,m^{-3}$, energy dissipation rates of 50 mW/kg, viscosity and collision frequencies computed at 84 km from neutral densities from the NRLMSISE-00 model and temperatures from Lübken (1999). An ion mass of 31 amu is assumed for freshly created auroral plasma. Ion-neutral

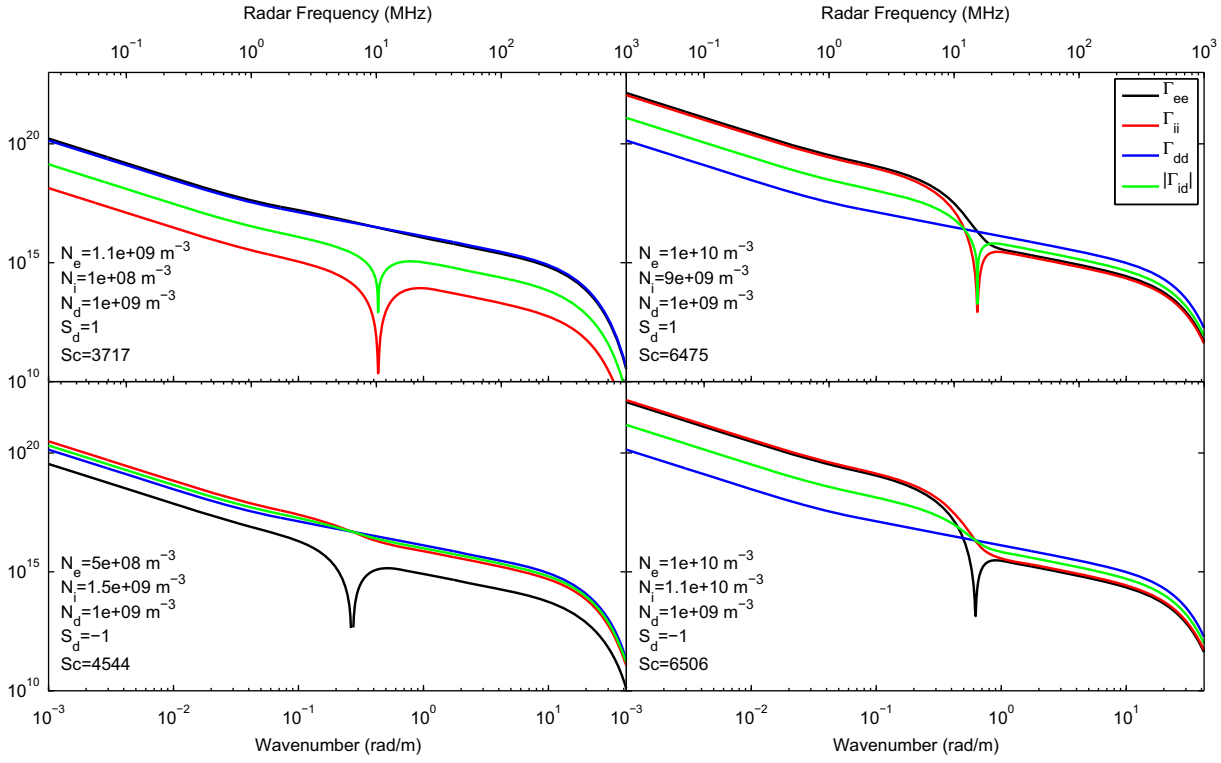

Fig. 10. Four examples of numerical solutions to the coupled ODEs derived by Hill et al. (1999). The densities and particle assumed dust charges for each example are printed in the lower left portion of each panel. See the text for all other parameters. The lower abscissa shows the wavenumber and the upper abscissa shows the frequency of the corresponding backscatter radar.

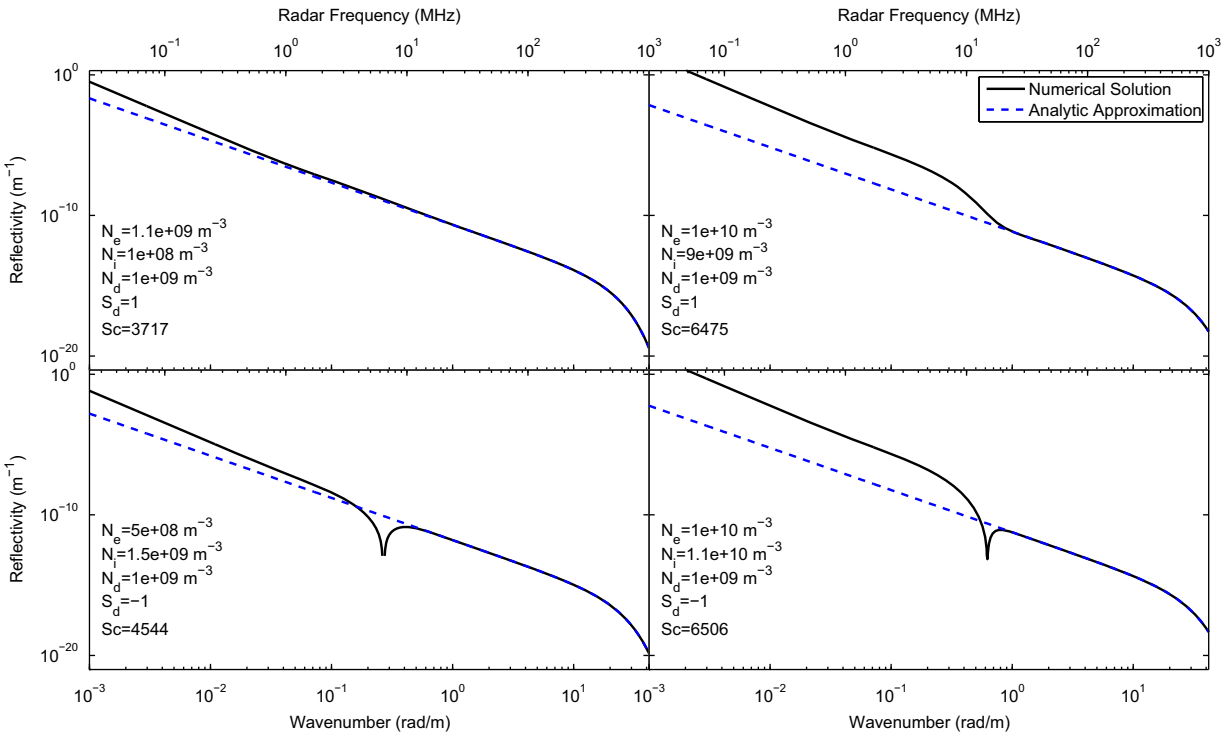

Fig. 11. Reflectivities corresponding to the examples in Fig. 10 along with the asymptotic solutions from Eq. (44).

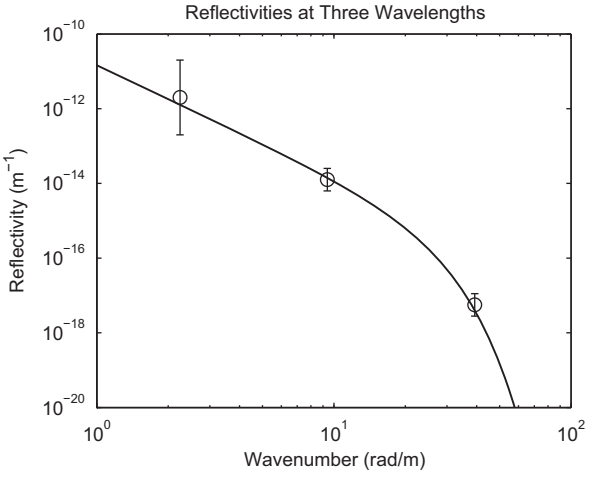

Fig. 12. Measured reflectivities at three wavelengths from Rapp et al. (2008) along with a fit using Eq. (44). See the text for the assumed parameters.

collision frequencies are again derived using the expression from Hill and Bowhill (1977), and dust particle collision frequencies are derived using an approximation of the hard sphere collision model (Schunk and Nagy, 2000; Strelnikova et al., 2007)

$$m_d \nu_{dn} \approx \tfrac{8}{3}(r_p + r_n)^2 N_n \sqrt{2\pi k_B T m_n}, \tag{49}$$

assuming a mean neutral radius of $r_n = 0.15$ nm and mass of $m_n = 4.8 \times 10^{-26}$ kg. The four examples differ in the sign of the dust charge and in the electron density. Thirty nm particles are expected to always charge negative in this region (Rapp and Lübken, 2001), but solutions for positive particles are shown as well to illustrate the behavior of these solutions. In each case the electron spectrum transitions from a $k^{-5/3}$ to a k^{-1} power law near k^* exactly like the spectrum for a neutral advected passive scalar, but at higher wavenumbers the shape is more complicated because it is the superposition of multiple eigenmodes. The first steep drop in the second example (upper right panel) is the result of the fast eigenmode transitioning into its viscous-diffusive subrange while the slow eigenmode remains in its viscous-convective subrange. Some of the variance generated at the largest scales gets dissipated in this drop, and only a portion gets convected out to the smallest scales. The narrow notches in the electron spectra for the two cases with negative particles are places where the various components are summing to zero, and occur slightly after the fast eigenmode transitions into its viscous-diffusive range. At these places the electrons' tendencies to follow positive ions and avoid negative dust are exactly canceling. This perfect cancellation is essentially an artifact of assuming perfect homogeneity, stationarity and isotropy. All four examples use the same size particle, and yet have different Schmidt numbers because D_2^0 is a function of the relative densities of the various species. The examples where the dust density is large compared to the ion density have nearly half the Schmidt number of the other examples because in this case the electrons are enhancing the dust diffusion, thus making D_2^0 nearly double D_d.

Fig. 11 shows the reflectivities corresponding to the four examples in Fig. 10 along with the asymptotic solutions computed using Eq. (44). In all four cases the asymptotic form agrees fantastically with the numerical solution in the VHF and UHF ranges.

The reflectivities reported by Rapp et al. (2008) at scales of 2.8 m, 67 cm, and 16 cm are compared to the asymptotic expression, Eq. (44), in Fig. 12. During this experiment the electron density, density gradient, and energy dissipation rate were estimated as $10^{10}\,\mathrm{m}^{-3}$, $3 \times 10^6\,\mathrm{m}^{-4}$, and 60 mW/kg, respectively. The neutral scale, H_n, is assumed to be 1 km as before. No measurements of the ice grain density, density gradient, or charge were possible. Fortunately these parameters only affect the magnitude of the entire curve and not the shape, and thus the Schmidt number can still be accurately estimated without them. For Fig. 12 values of $N_d = 10^9\,\mathrm{m}^{-3}$, $dN_d/dz = 2.25 \times 10^6\,\mathrm{m}^{-4}$, and $Z_d = -1$ have been assumed arbitrarily and give reasonable agreement with the data. There

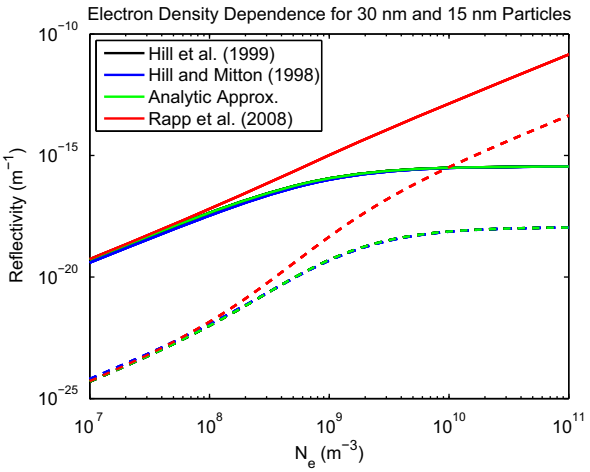

Fig. 13. Reflectivity at PFISR's wavenumber as a function of electron density for 30 nm particles at 84 km (solid lines) and 15 nm particles at 86 km (dashed lines). See the text for all other parameters. Numerical solutions to the coupled ODEs derived by Hill and Mitton (1998) and Hill et al. (1999) both without (black lines) and with (blue lines) the finite Debye length correction agree well with the results of Eq. (44) (green lines). The reflectivities computed using the expression from Rapp et al. (2008) (red lines) are clearly inappropriate in the high electron density regime. (For interpretation of the references to color in this figure legend, the reader is referred to the web version of this article.)

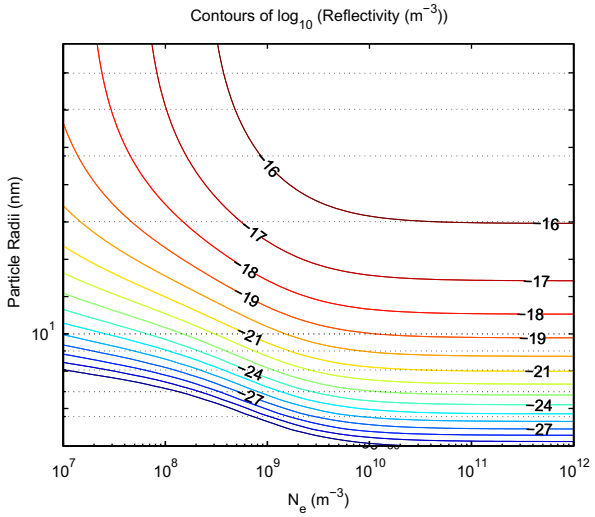

Fig. 14. Contours of constant reflectivity at 84 km as a function of particle size and electron density. All other parameters are the same as in the previous figures. The orange curve corresponding to $10^{-19}\,\mathrm{m}^{-1}$ is approximately PFISR's detection limit. (For interpretation of the references to color in this figure legend, the reader is referred to the web version of this article.)

are an infinite set of different choices for these three parameters which will all give equally satisfactory agreement with the data, and thus no information about any one of these parameters can actually be extracted. Fig. 12 uses an assumed particle radius of 30 nm, which corresponds to a Schmidt number of 6506 for the assumed densities and charges and a viscosity of $1\,\mathrm{m}^2/\mathrm{s}$. We require a Schmidt number which is over twice as large as the estimate of ~ 2500 given by Rapp et al. (2008) to fit the same data because we have chosen a different value of the Batchelor constant, q, and the shape of the curve depends on the ratio q/Sc. Rapp et al. (2008) follows Batchelor (1959) and uses $q=2$ whereas we have followed Hill and Mitton (1998) and used $q=4.08$. The certainty of Schmidt number estimates from multiple wavelength studies such as Rapp et al. (2008); Li et al. (2010) is limited by knowledge of this constant.

Fig. 13 illustrates the electron density dependence of the reflectivity for 30 nm particles at 84 km (solid lines) and 15 nm particles at 86 km (dashed lines). The black lines are numerical solutions to Eq. (31) using Eq. (20), the blue lines are numerical solutions to a slightly more general form of these equations which include a finite electron Debye length (Hill and Mitton, 1998), the green lines are computed from Eq. (44), and the red lines use the expression derived by Rapp et al. (2008). The dust is assumed to be singly negatively charged and all other parameters are the same as in the previous examples. In both cases the reflectivity scales with electron density at low electron densities, but at high electron densities the reflectivity becomes independent of electron density. Both of these attributes are easily seen from Eq. (44). For $Z_d=-1$ and $Z_i=1$ the term $\overline{S}$ reduces to $1/(2+\Lambda)$, where in this case $\Lambda=N_d/N_e$. For high electron densities (low Λ) this term is simply 1/2 so the reflectivity is solely controlled by the dust density through χ_{dd}. For low electron densities (high Λ) this term becomes $1/\Lambda=N_e/N_d$, thus implying a strong electron density dependence. This concisely explains how PMSE reflectivity can appear to be independent of electron density while still necessarily going to zero in the absence of free electrons.

Changes in electron density can also change the reflectivity by changing D_2^0 by as much as a factor of 2, and the importance of this effect depends on how large the particles are. This is why the curves for 15 nm particles in Fig. 13 are considerably more complicated than those for 30 nm particles. For large particles PFISR's wavenumber is comfortably in the viscous-convective subrange, meaning that exponential term in Eq. (44) is nearly 1. Smaller particles, however, could be in the viscous-diffusive subrange, meaning the exponential term is significantly less than 1. In this case variations in D_2^0 by as little as a factor of 2 can translate into orders of magnitude of variation in the reflectivity. Changes in the number of charges on each particle could magnify this effect and are worthy of further investigation.

Contours of constant reflectivity computed from Eq. (44) as a function of particle size and electron density are plotted in Fig. 14. The altitude is fixed at 84 km and all other parameters are the same as in the previous examples. For large electron densities and large particles there is clearly a plateau where both the electron density and particle size have no effect. The limiting reflectivity of this plateau is given by taking the exponential term in Eq. (44) to be 1 and the $\overline{S}=1/2$:

$$\eta_{max}=2\pi^3 r_e^2\frac{f_x qRi}{Pr^t\omega_B^2}\sqrt{\varepsilon\nu_a}\left(\frac{\omega_B^2 N_d}{g}-\frac{dN_d}{dz}-\frac{N_d}{H_n}\right)^2 k^{-3}. \tag{50}$$

For the parameters used here this value is $9.6\times10^{-16}\,\mathrm{m}^{-1}$.

The sensitivity threshold of PFISR varies depending on experimental conditions, but is nominally a reflectivity of $10^{-19}\,\mathrm{m}^{-1}$, which corresponds to incoherent scatter from an electron density of $2\times10^9\,\mathrm{m}^{-3}$. From Fig. 14 it is clear that for larger particles there is a sizable region where the PMSE will be detectable but incoherent scatter from electrons will be well below the detection limit. Thus the observations of PMSE at night with no detectable incoherent scatter can still be explained by scattering from free electrons.

The seemingly contradictory observations of PMSE being modulated by electron density variations in a high layer while simultaneously ignoring electron density variations in a lower layer can be completely understood in terms of Eq. (44). The lower layer has a high electron density and large particles, so the reflectivity there is completely decoupled from the electron density. The higher layer presumably has smaller particles, and thus the variations in D_2^0 have a strong effect and the PMSE can be modulated on and off by the electron density.

6. Conclusions

We have presented several examples of PMSE observed in drastically different electron density conditions which are difficult to interpret by assuming that the echo strength scales with electron density. These include the observations of PMSE at night with no detectable electron density nearby and PMSE during aurora which show little or no response to the varying particle precipitation. These observations show that expressions which suggest that the reflectivity scales with N_e (e.g. Cho, 1993; Rapp et al., 2008) cannot be correct. Nonetheless, all of the observations can still be explained as scatter from free electrons which are structured by neutral turbulence and coupled to heavy ice grains through the ambipolar electric field. The rigorous treatments of turbulent spectra in ionized gases with an arbitrary number of charged species by Hill and Mitton (1998) and Hill et al. (1999) predict a much more complicated dependence on electron density. We have derived an analytic solution to the system of equations derived by Hill et al. (1999) in the high wavenumber limit which makes the dependency more clear. The expression for reflectivity corresponding to this solution, i.e. Eq. (44), is identical to that derived by Rapp et al. (2008) except the leading term involving the electron density and density gradient has been replaced by a term involving the dust density and density gradient and the relative densities of electrons and dust. Mathematically this change arises from applying the boundary conditions in the inertial subrange with all of the eigenmodes included. Some of the electron density variations generated at the largest scales will be dissipated by the faster eigenmodes and only a fraction will be convected out to the small scales responsible for PMSE at VHF and UHF. When the electron density is much greater than the dust density the reflectivity only depends on the dust density, thus explaining the observations of PMSE which do not respond to aurora. PMSE which do respond to aurora are probably somewhat into the viscous-diffusive subrange where variations in electron density can change the reflectivity by orders of magnitude by changing the slow ambipolar diffusion coefficient. This case is more likely for smaller particles and at the highest UHF frequencies used to observe PMSE. When the electron density is much smaller than the dust density the reflectivity is a strong function of the electron density and will go to zero in the absence of free electrons. The observations of PMSE at night with no detectable incoherent scatter do not suggest that PMSE can exist without free electrons, however. The region in the top left corner of Fig. 14 illustrates that for 30–50 nm particles the reflectivity can be detectable even for electron densities as low as $10^8\,m^{-3}$, which is well below PFISR's detection limit for incoherent scatter.

Acknowledgements

The Poker Flat Incoherent Scatter Radar is operated by SRI International under NSF cooperative agreement ATM-0608577. Work at Cornell is supported by the NSF under Grants ATM-0551107 and ATM-0538343. Work at the University of Alaska Fairbanks is supported by the NSF under Grant ARC-0632387. The authors thank the staff at the Poker Flat Research Range for their support.

References

Batchelor, G.K., 1959. Small-scale variation of convected quantities like temperature in a turbulent fluid: part 1. General discussion of the case of small conductivity. J. Fluid Mech. 5, 113–133.

Bellan, P.M., 2008. Ice iron/sodium film as cause for high noctilucent cloud radar reflectivity. J. Geophys. Res. 113, D16215.

Berger, U., von Zahn, U., 2002. Icy particles in the summer mesopause region: three-dimensional modeling of their environment and two-dimensional modeling of their transport. J. Geophys. Res. 107 (A11), 1366.

Bremer, J., Hansen, T.L., Hoffmann, P., Latteck, R., 2001. Dependence of polar mesosphere summer echoes on solar and geomagnetic activity. Adv. Space Res. 28, 1071–1076.

Bremer, J., Hoffmann, P., Hansen, T.L., 2000. Geomagnetic control of polar mesosphere summer echoes. Ann. Geophys. 18, 202–208.

Burns, C.J., Turunen, E., Matveinen, H., Ranta, H., Hargreaves, J.K., 1991. Chemical modelling of the quiet summer D- and E-regions using EISCAT electron density profiles. J. Atmos. Terr. Phys. 53, 115–134.

Cho, J.Y.N., 1993. Radar scattering from the summer polar mesosphere: theory and observations. Ph.D. Thesis, Cornell University.

Cho, J.Y.N., Kelley, M.C., Heinselman, C.J., 1992a. Enhancement of Thomson scatter by charged aerosols in the polar mesosphere: measurements with a 1.29 GHz radar. Geophys. Res. Lett. 19, 1097–1100.

Cho, J.Y.N., Hall, T.M., Kelley, M.C., 1992b. On the role of charged aerosols in polar mesosphere summer echoes. J. Geophys. Res. 97, 875–886.

Collins, R.L., Kelley, M.C., Nicolls, M.J., Ramos, C., Hou, T., Stern, T.E., Mizutani, K., Itabe, T., 2003. Observations of a noctilucent cloud and an internal wave in the polar mesosphere. J. Geophys. Res. 108, 8435.

Collins, R.L., Taylor, M.J., Nielsen, K., Mizutani, K., Murayama, Y., Sakanoi, K., De Land, M.T., 2009. Noctilucent clouds in the western Arctic in 2005: simultaneous lidar and camera observations an analysis. J. Atmos. Sol. Terr. Phys. 71, 446–452.

Corrsin, S., 1964. Further generalization of Onsager's cascade model for turbulent spectra. Phys. Fluids 7, 1156–1159.

Czechowsky, P., Rüster, R., Schmidt, G., 1979. Variations of mesospheric structures in different seasons. Geophys. Res. Lett. 6, 459–462.

del Pozo, C.F., Hargreaves, J.K., Aylward, A.D., 1997. Ion composition and effective ion recombination rate in the nighttime aurora1 lower ionosphere. J. Atmos. Sol. Terr. Phys. 59, 1919–1943.

Dougherty, J.P., Farley, D.T., 1963. A theory of incoherent scattering of radio waves by a plasma: 3. Scattering in a partly ionized gas. J. Geophys. Res. 68, 5473–5486.

Ecklund, W.L., Balsley, B.B., 1981. Long term observations of the arctic mesosphere with the MST radar at Poker Flat, Alaska. J. Geophys. Res. 86, 7775–7780.

Fritts, D.C., Alexander, M.J., 2003. Gravity wave dynamics and effects in the middle atmosphere. Rev. Geophys. 41, 1003–1066.

Gadsden, M., 1990. A secular change in noctilucent cloud occurrence. J. Atmos. Terr. Phys. 52, 247–251.

Gibson, C.H., 1968. Fine structure of scalar fields mixed by turbulence: II. Spectral theory. Phys. Fluids 11, 2316–2327.

Hagfors, T., 1992. Note on the scattering of electromagnetic waves from charged dust particles in a plasma. J. Atmos. Terr. Phys. 54, 333–338.

Hall, C.M., Röttger, J., 2001. Initial observations of polar mesospheric summer echoes using the EISCAT Svalbard Radar. Geophys. Res. Lett. 28, 131–134.

Havnes, O., Brattli, A., Aslaksen, T., Singer, W., Latteck, R., Blix, T., Thrane, E., Trøim, J., 2001. First common volume observations of layered plasma structures and polar mesospheric summer echeos by rocket and radar. Geophys. Res. Lett. 28, 1419–1422.

Havnes, O., Trøim, J., Blix, T., Mortensen, W., Næsheim, L.I., Thrane, E., Tønnesen, T., 1996. First detection of charged dust particles in the Earth's mesosphere. J. Geophys. Res. 101, 10839–10847.

Hedin, A.E., 1991. Extension of the MSIS thermosphere model into the middle and lower atmosphere. J. Geophys. Res. 96, 1159–1172.

Hervig, M.E., Gordley, L.L., Russell, J.M., Bailey, S.M., 2009. SOFIE PMC observations during the northern summer of 2007. J. Atmos. Sol. Terr. Phys. 71, 331–339.

Hill, R.J., 1978a. Nonneutral and quasi-neutral diffusion of weakly ionized multiconstituent plasma. J. Geophys. Res. 83, 989–998.

Hill, R.J., 1978b. Models of the scalar spectrum for turbulent advection. J. Fluid Mech. 88, 541–562.

Hill, R.J., Bowhill, S.A., 1976. Small-scale fluctuations in D-region ionization due to hydrodynamic turbulence. Aeronomy Report 75, Department of Electrical Engineering, University of Illinois, Urbana, IL.

Hill, R.J., Bowhill, S.A., 1977. Collision frequencies for use in the continuum momentum equations applied to the lower ionosphere. J. Atmos. Terr. Phys. 39, 803–811.

Hill, R.J., Clifford, S.F., 1978. Modified spectrum of atmospheric temperature fluctuations and its application to optical propagation. J. Opt. Soc. Am. 68, 892–899.

Hill, R.J., Gibson-Wilde, D.E., Werne, J.A., Fritts, D.C., 1999. Turbulence induced fluctuations in ionization and application to PMSE. Earth Planets Space 51, 499–513.

Hill, R.J., Mitton, K.A., 1998. Turbulence-induced ionization fluctuations in the lower ionosphere. Technical Report ERL 454-ETL 68, NOAA, November.

Hines, C.O., 1960. Internal atmospheric gravity waves at ionospheric heights. Can. J. Phys. 38, 1441–1481.

Hocking, W.K., 1985. Measurement of turbulent energy dissipation rates in the middle atmosphere by radar techniques: a review. Radio Sci. 20, 1403–1422.

Kelley, M.C., Farley, D.T., Röttger, J., 1987. The effect of cluster ions on anomalous VHF backscatter from the summer polar mesosphere. Geophys. Res. Lett. 14, 1031–1034.

Kelley, M.C., Nicolls, M.J., Varney, R.H., Collins, R.L., Doe, R., Plane, J.M.C., Thayer, J., Taylor, M., Thurairajah, B., Mizutani, K., 2010. Radar lidar and optical

observations in the polar summer mesosphere shortly after a space shuttle launch. J. Geophys. Res. 115, A05304.
La Hoz, C., 1992. Radar scattering from dusty plasmas. Phys. Scr. 45, 529–534.
Li, Q., Rapp, M., Röttger, J., Latteck, R., Zecha, M., Strelnikova, I., Baumgarten, G., Hervig, M., Hall, C., Tsutsumi, M., 2010. Microphysical parameters of mesospheric ice clouds derived from calibrated observations of polar mesospheric summer echoes at Bragg wavelengths of 2.8 m and 30 cm. J. Geophys. Res. 115, D00I13.
Lübken, F.-J., 1992. On the extraction of turbulent parameters from atmospheric density fluctuations. J. Geophys. Res. 97, 20385–20395.
Lübken, F.-J., 1999. Thermal structure of the Arctic summer mesosphere. J. Geophys. Res. 104, 9135–9149.
Lübken, F.-J., Rapp, M., Hoffmann, P., 2002. Neutral air turbulence and temperatures in the vicinity of polar mesosphere summer echoes. J. Geophys. Res. 107.
Nicolls, M.J., Heinselman, C.J., Hope, E.A., Ranjan, S., Kelley, M.C., Kelly, J.D., 2007. Imaging of polar mesosphere summer echoes with the 450-mHz Poker Flat Advanced Modular Incoherent Scatter Radar. Geophys. Res. Lett. 34.
Nicolls, M.J., Kelley, M.C., Varney, R.H., Heinselman, C.J., 2009. Spectral observations of polar mesospheric summer echoes at 33 cm (450 MHz) with the Poker Flat Incoherent Scatter Radar. J. Atmos. Sol. Terr. Phys. 71, 662–674.
Nicolls, M.J., Varney, R.H., Vadas, S.L., Kelley, M.C., Stamus, P., Heinselman, C.J., in press. Influence of an inertia-gravity wave on mesospheric dynamics: a case study with the Poker Flat Incoherent Scatter Radar. J. Geophys. Res , doi:10.1029/2010JD014042.
Onsager, L., 1949. Statistical hydrodynamics. Nuovo Cimento Suppl. 6, 279–287.
Ottersten, H., 1969. Radar backscattering from the turbulent clear atmosphere. Radio Sci. 4, 1251–1255.
Pao, Y.-H., 1965. Structure of turbulent velocity and scalar fields at large wavenumbers. Phys. Fluids 8, 1063–1075.
Picone, J.M., Hedin, A.E., Drob, D.P., Aikin, A.C., 2002. NRLMSISE-00 empirical model of the atmosphere: statistical comparisons and scientific issues. J. Geophys. Res. 107, 1468.
Rapp, M., Gumbel, J., Lübken, F.-J., Latteck, R., 2002a. *D* region electron number density limits for the existence of polar mesosphere summer echoes. J. Geophys. Res. 107 (D14).
Rapp, M., Lübken, F.-J., Müllemann, A., Thomas, G.E., Jensen, E.J., 2002b. Small-scale temperature variations in the vicinity of NLC: experimental and model results. J. Geophys. Res. 107, 4392.
Rapp, M., Lübken, F.-J., 2001. Modelling of particle charging in the polar summer mesosphere: 1. General results. J. Atmos. Sol. Terr. Phys. 63, 759–770.
Rapp, M., Lübken, F.-J., 2003. On the nature of PMSE: electron diffusion in the vicinity of charged particles revisited. J. Geophys. Res. 108.
Rapp, M., Lübken, F.-J., 2004. Polar mesosphere summer echoes (PMSE): review of observations and current understanding. Atmos. Chem. Phys. 4, 2601–2633.
Rapp, M., Lübken, F.-J., 2009. Comment on "Ice iron/sodium film as cause for high noctilucent cloud radar reflectivity" by P.M. Bellan. J. Geophys. Res. 114, D11204.
Rapp, M., Strelnikova, I., Latteck, R., Hoffman, P., Hoppe, U.-P., Häggström, I., Rietveld, M., 2008. Polar mesosphere summer echoes (PMSE) studied at Bragg wavelengths of 2.8 m, 67 cm, and 16 cm. J. Atmos. Sol. Terr. Phys. 70, 947–961.
Robertson, S., Horányi, M., Knappmiller, S., Sternovsky, Z., Holzworth, R., Shimogawa, M., Friedrich, M., Torkar, K., Gumbel, J., Megner, L., Baumgarten, G., Latteck, R., Rapp, M., Hoppe, U.-P., Hervig, M.E., 2009. Mass analysis of charged aerosol particles in NLC and PMSE during the ECOMA/MASS campaign. Ann. Geophys. 27, 1213–1232.
Röttger, J., Hoz, C.L., Kelley, M.C., Hoppe, U.P., Hall, C., 1988. The structure and dynamics of polar mesosphere summer echoes observed with the EISCAT 224 MHz radar. Geophys. Res. Lett. 15, 1353–1356.
Röttger, J., Rietveld, M.T., La Hoz, C., Hall, C., Kelley, M.C., Swartz, W.E., 1990. Polar mesosphere summer echoes observed with the EISCAT 933-MHz radar and the CUPRI 46.9-MHz radar, their similarity to 224-MHz radar echoes, and their relation to turbulence and electron density profiles. Radio Sci. 25, 671–687.
Røyvick, O., Smith, L.G., 1984. Comparison of mesospheric VHF radar echoes and rocket probe electron concentration measurements. J. Geophys. Res. 89, 9014–9022.
Schunk, R.W., Nagy, A.F., 2000. Ionospheres: Physics, Plasma Physics, and Chemistry. Cambridge University Press.
Strelnikova, I., Rapp, M., Raizada, S., Sulzer, M., 2007. Meteor smoke particle properties derived from arecibo incoherent scatter radar observations. Geophys. Res. Lett. 34, L15185.
Tatarski, V.I., 1961. Wave Propagation in a Turbulent Medium. McGraw-Hill Book Company, Inc.
Taylor, M.J., Zhao, Y., Pautet, P.-D., Nicolls, M.J., Collins, R.L., Barker-Tvedtnes, J., Burton, C.D., Thurairajah, B., Reimuller, J., Varney, R.H., Heinselman, C.J., Muzutani, K., 2009. Coordinated optical and radar image measurements of noctilucent clouds and polar mesospheric summer echoes. J. Atmos. Sol. Terr. Phys. 71, 675–687.
Thurairajah, B., Collins, R.L., Mizutani, K., 2009. Multi-year temperature measurements of the middle atmosphere at Chatanika Alaska (65°N, 147°W). Earth Planets Space 61, 755–764.
Varney, R.H., Nicolls, M.J., Heinselman, C.J., Kelley, M.C., 2009. Observations of polar mesospheric summer echoes using PFISR during the summer of 2007. J. Atmos. Sol. Terr. Phys. 71, 470–476.
von Zahn, U., Bremer, J., 1999. Simultaneous and common-volume observations of noctilucent clouds and polar mesosphere summer echoes. Geophys. Res. Lett. 26, 1521–1524.